Supplementary Information for

Magnetic field Enhancement of $FeCoSe_2$ Photoanode for the Oxygen Evolution Reaction by Adjusting Hole Density to Reduce Competitive Adsorption between Fe and Co in Photoelectrochemical Water-Splitting System

Ben Fan[a], Zebin Yu[*a], Ling Ding[a], Ronghua Jiang[b], Yanping Hou[a], Shuang Li[c], Jianhua Chen[a]*

[a] State Key Laboratory of Featured Metal Materials and Life-cycle Safety for Composite Structures, School of Resources, Environment and Materials, Guangxi University, Nanning 530004, P.R.China.

[b] School of Chemical and Environmental Engineering, Shaoguan University, Shaoguan 512005, P. R. China.

[c] School of Environmental Science and Technology, Dalian University of Technology, Dalian 116023, PR China

[*] Corresponding author.

Tel.: + 8613877108420 (Z. Yu)

E-mail: xxzx7514@hotmail.com (Z. Yu)

1. Experimental section

1.1. Characterization

In order to analyze the crystalline structure, the samples were characterized by X-ray diffraction (XRD) using Bruker D8 XRD Goniomerter with Cu Kα radiation in the range of 20° to 70°, Refinement of XRD was accomplished by GSAS-II. The morphologies of the samples were determined with a field emission scanning electron microscopy (FESEM, Hitachi SU8020), Elemental analysis of the samples was conducted by an energy dispersive X-ray spectrometer (EDS) attached to scanning electron microscopy (SEM). Transmission electron microscopy (TEM, FEI Talos F200X) and a high-resolution transmission electron microscopy (HRTEM). The chemical state of the samples was analysed by an X-ray photoelectron spectroscopy (XPS, Thermo ESCALAB 250XI). The magnetic properties of the samples were tested by a vibrating sample magnetometer (VSM, 7410). UV–visible diffuse reflectance spectra (UV-vis DRS) were measured using a Shimadzu UV-3600 plus spectrometer with $BaSO_4$-coated integration sphere in the region of 200-800 nm. The photoluminescence spectra for the samples were investigated on a steady-state fluorescence spectrometer (PL, OmniFluo-960) with an excitation wave length of 382 nm.

1.2. Photoelectrochemical measurements

All the photoelectrochemical measurements were measured on a CHI660E electrochemical work station (Chenhua Instrument, Shanghai, China) with a standard

three electrode system. The adopted illumination source was simulated sunlight (100 mW cm^{-2}) from a 300 W Xe lamp (CEL-HXF300F3, AM 1.5G, Beijing China Education Au-light Co., Ltd., China), and 1 M KOH (pH 13.6) was used as electrolyte.

Linear sweep voltammetry (LSV) characteristics were monitored by scanning potential from 0 to 0.6 V vs. SCE at a scan rate of 10 mV s^{-1} with 95% IR compensation. The measured potentials were converted to the reversible hydrogen electrode (RHE) scale using the equation (1)

$$E_{RHE}=E_{SCE}+0.059\times pH + 0.098V \quad (1)$$

where E_{SCE} is the experimentally measured potential (0.098 V vs. SCE at 25 °C).

Electrochemical impedance spectroscopy (EIS) was employed to evaluate the electroconductibility of prepared photoanodes. EIS spectra were obtained with AC voltage amplitude of 10 mV at a DC bias from 0 to 0.6 V (vs. Hg/HgO), under AM 1.5 G illuminations, where the frequency range was set at 0.01 Hz~100 kHz.

The incident photon to current efficiency (IPCE) was obtained using a 300 W Xe lamp equipped with different monochromators and was measured in 1 M KOH (pH 13.6) at 1.23 VRHE using a three-electrode setup like that for photocurrent measurements. IPCE was calculated according to the equation (2):

$$\text{IPCE (\%)} = \frac{(J_{dark} - J_{light}) \times 1240}{(\lambda \times P)} \times 100\% \quad (2)$$

where J refers to the photocurrent density (mA cm^{-2}) obtained from the electrochemical workstation at 1.23 VRHE, λ is the incident light wavelength (nm) provided by the specific monochromator, P is the incident light intensity (mW cm^{-2}).

Applied bias photon-to-current efficiency (ABPE) was calculated using the following equation (3):

$$\text{ABPE (\%)} = \frac{J \times (1.23 - Vb)}{Ptotal} \times 100\% \quad (3)$$

where J refers to the photocurrent density (mA cm^{-2}) obtained from the electrochemical workstation, Vb is the applied bias vs RHE (V), and Ptotal is the total light intensity of AM 1.5 G (100 mW cm^{-2}).

$$\eta_{inj} = \frac{J_{H_2O}}{J_{Na_2SO_3}} \times 100\% \quad (4)$$

$$\eta_{sep} = \frac{J_{Na_2SO_3}}{J_{abs}} \times 100\% \quad (5)$$

Where J_{H2O} and J_{Na2SO3} are the photocurrent density measured in queous solution without and with Na_2SO_3 as a hole scavenger, respectively. J_{abs} is the photon absorption rate expressed as the photocurrent density. J_{abs} of $FeCoSe_2$ is equal to 7.74 mA cm^{-2}.

1.3 Density function theory calculation details

Electronic properties of nanomaterials at the atomic level can be efficiently calculated using Density functional theory (DFT). In this work, the structural and electronic properties of the prepared $FeSe_2$, $CoSe_2$ and $FeCoSe_2$ catalyst have been studied using the DFT-based CASTEP and DMOL3 tools. In these tools, the first-principles DFT calculation with Norm Conserving (NC) pseudo-potential has been implemented using the Pardew-Burke-Ernzerhof generalized gradient approximation (PBE-GGA) method, and interaction between core electrons and valence electrons described using the frozen-core projector-augmented wave (PAW) method. All calculations were employed with a plane-wave cutoff energy of 400 eV. 10-5 eV was

fixed as the convergence criterion for the self-consistency (SC) process, and 0.02 eV/Å was assumed to calculate the total energy. The GGA + U calculations are performed using the model proposed by RenXiao et al.[1], with the Ueff (Ueff = Coulomb U – exchange J) values of 3.3 eV and 4 eV for Co and Fe, respectively.

Slab model with using (111) surface for all samples, $FeSe_2$, $CoSe_2$ and $FeCoSe_2$ were considered to calculate adsorption energy and vacuum slabs of 15 Å along the normal direction were fixed for all samples to avoid interactions between adjacent layers. Further, for the density of states (DOS) calculations of $FeSe_2$, $CoSe_2$ and $FeCoSe_2$ models, a 1 × 1 × 1 super cell is employed and the Γ-point-centered k-point meshes used for the Brillouin zone integrations were 3 × 3 × 2 k-points.

The adsorption energy was computed using the following equation,

$$E_{ad} = E_{ads/slab} - E_{ads} - E_{ads} \quad (6)$$

Where $E_{ads/slab}$, E_{slab}, and E_{ads} are the total energies for adsorbate on the slab, slab without adsorbate, and on adsorbate, respectively.

Mechanism for alkaline oxygen evolution reaction. The typically four-eletron transfer mechanistic for OER in alkaline solution pathway on catalysts films are generally considered as in the following Eq. (5) ~ (9):

$$M + OH^- \rightarrow M\text{-}OH + e^- \quad (7)$$

$$M\text{-}OH + OH^- \rightarrow M\text{-}O + H_2O + e^- \quad (8)$$

$$M\text{-}O + OH^- \rightarrow M\text{-}OOH + e^- \quad (9)$$

$$M\text{-}OOH + OH^- \rightarrow MO_2 + H_2O + e^- \quad (10)$$

$$MO_2 \rightarrow M + O_2 \quad (11)$$

M is a catalytically active surface site.

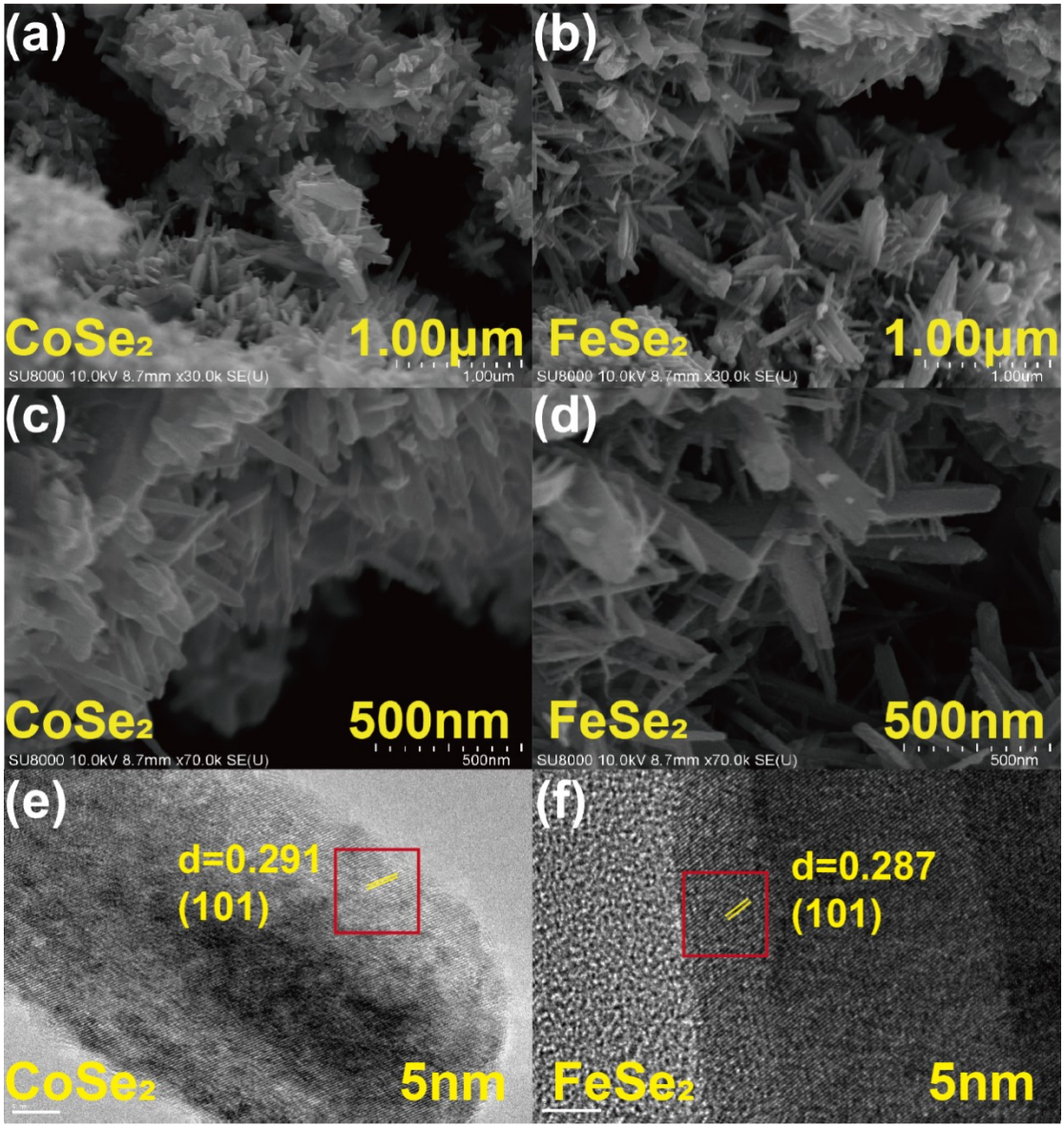

Figure. S1. (a,c) Scanning electron microscope (SEM) image of $CoSe_2$. (b,d) Scanning electron microscope (SEM) image of $FeSe_2$. (e) High-resolution transmission electron microscopy (HRTEM) image of $CoSe_2$. (f) High-resolution transmission electron microscopy (HRTEM) image of $FeSe_2$.

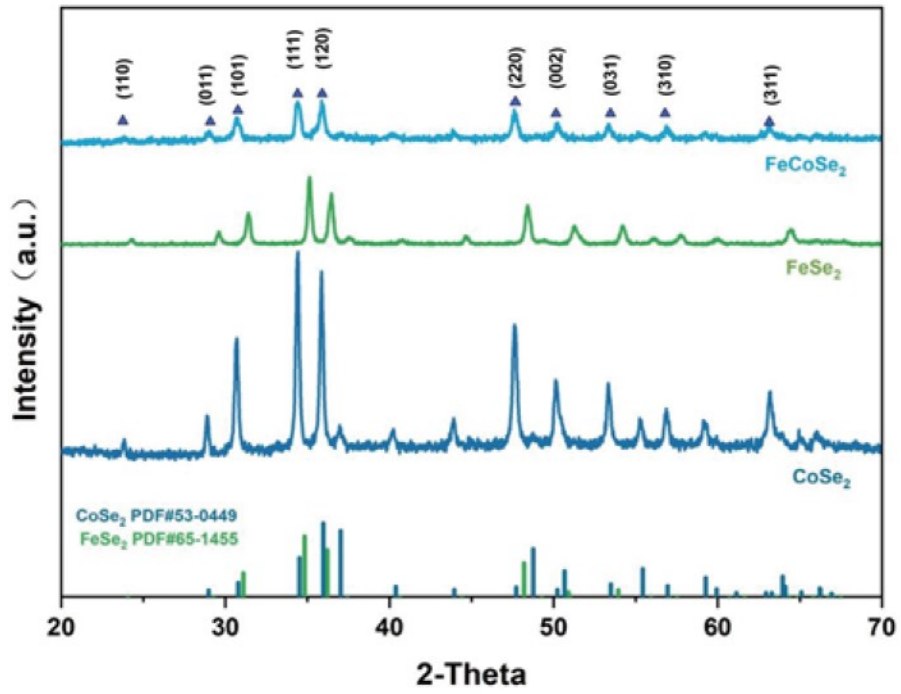

Figure. S2. XRD patterns of the $FeCoSe_2$, $FeSe_2$ and $CoSe_2$.

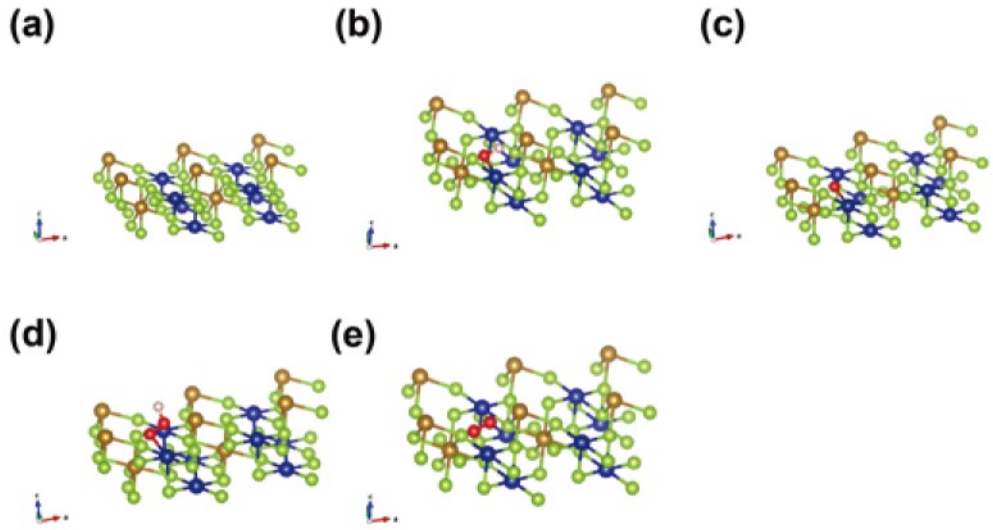

Figure. S3. (a) Surface adsorption model of M. (b) Surface adsorption model of M-OH. (c) Surface adsorption model of M-O. (d) Surface adsorption model of M-OOH. (e) Surface adsorption model of M, O_2.

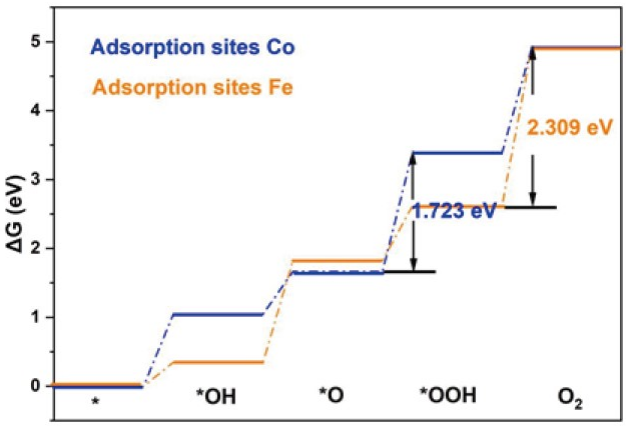

Figure. S4. OER Gibbs free energy diagrams of four-step reactions on $FeCoSe_2$ with different adsorption sites (Co or Fe).

We compared the Gibbs free energies of different metals as the active sites of the reactions. The Gibbs free energy of the decisive step required for Co as the reactive site was found to be lower than that of Fe. So we think Co could be the main reactive site, but this does not mean that the OER reaction takes place only at the Co site.

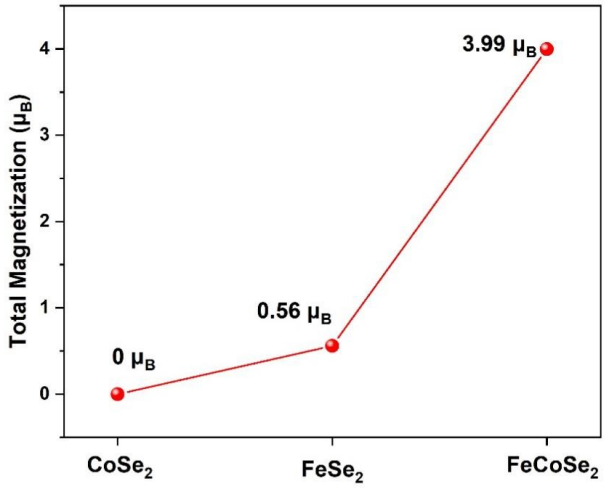

Figure. S5. Total magnetization of $CoSe_2$, $FeSe_2$ and $FeCoSe_2$.

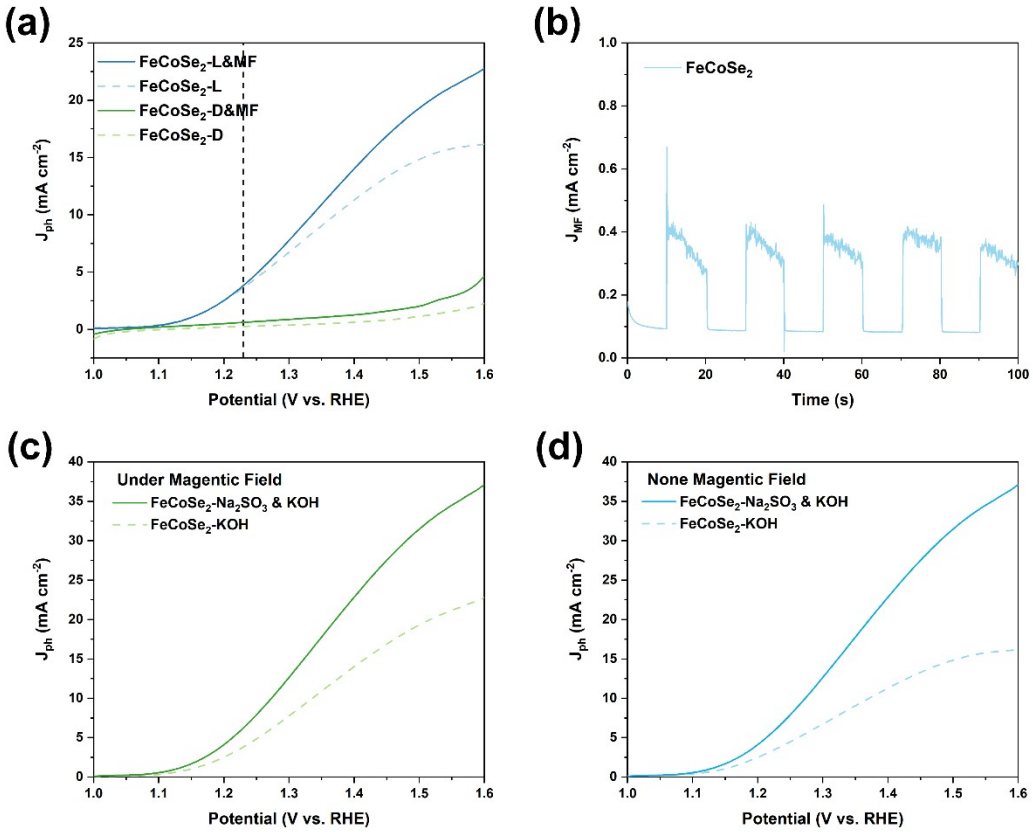

Figure. S6. (a) LSV of $FeCoSe_2$ photoanode in dark, dark & magnetic field, light and light & magnetic field conditions. (b) I-t of $FeCoSe_2$ photoanode in dark, dark & magnetic field conditions. (c, d) LSV of $FeCoSe_2$ (MF and NMF) in 1M KOH, 0.2M Na_2SO_3 and 1M KOH.

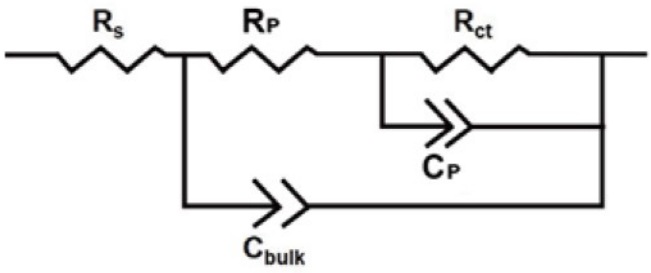

Figure. S7. Equivalent circuit used to fit impedance spectroscopy data for EIS Measurements.

Rs represents solution resistance, R_p represents the resistance from polarizing effects, R_{ct} represents the charge transfer resistance of the material surface, C_{bulk} represents the material bulk capacitance, C_p represents the material bulk capacitance.

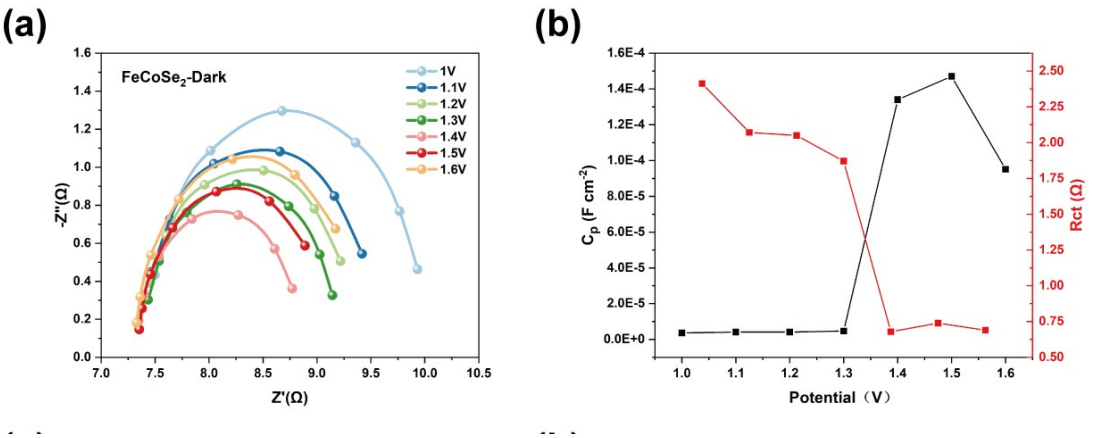

Figure. S8. (a) EIS fits at different voltages (1.0~1.6V vs RHE) under dark conditions. (b) Cp polarization capacitance and Rct surface charge transfer resistance obtained from fitted data under dark conditions.

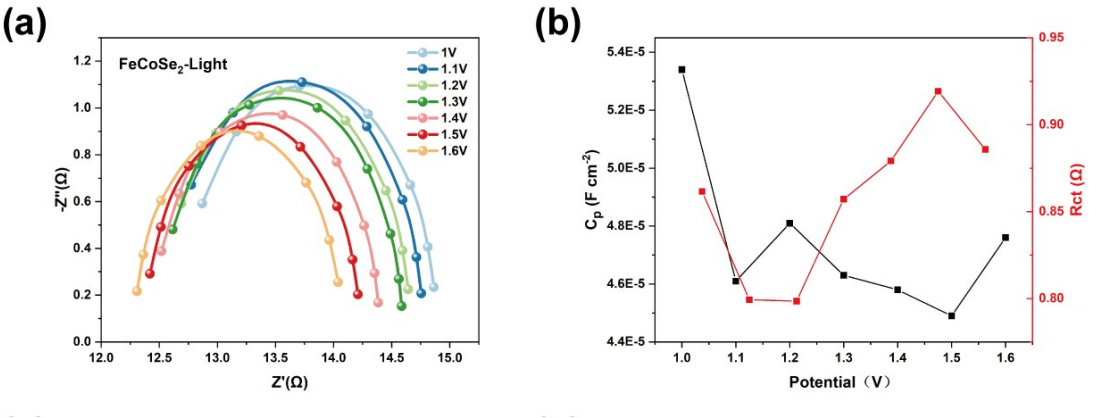

Figure. S9. (a) EIS fits at different voltages (1.0~1.6V vs RHE) under light conditions. (b) Cp polarization capacitance and Rct surface charge transfer resistance obtained from fitted data under light conditions.

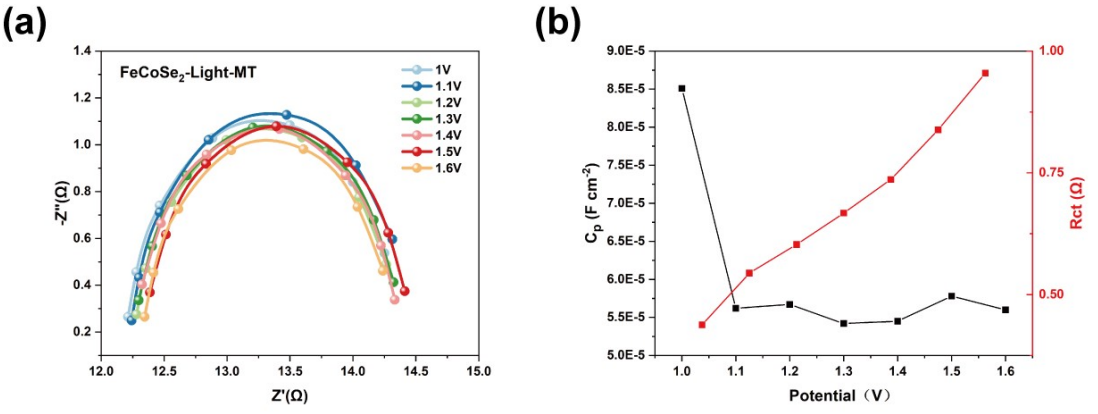

Figure. S10. (a) EIS fits at different voltages (1.0~1.6V vs RHE) under dark conditions. (b) Cp polarization capacitance and Rct surface charge transfer resistance obtained from fitted data under light and magnetic fields conditions.

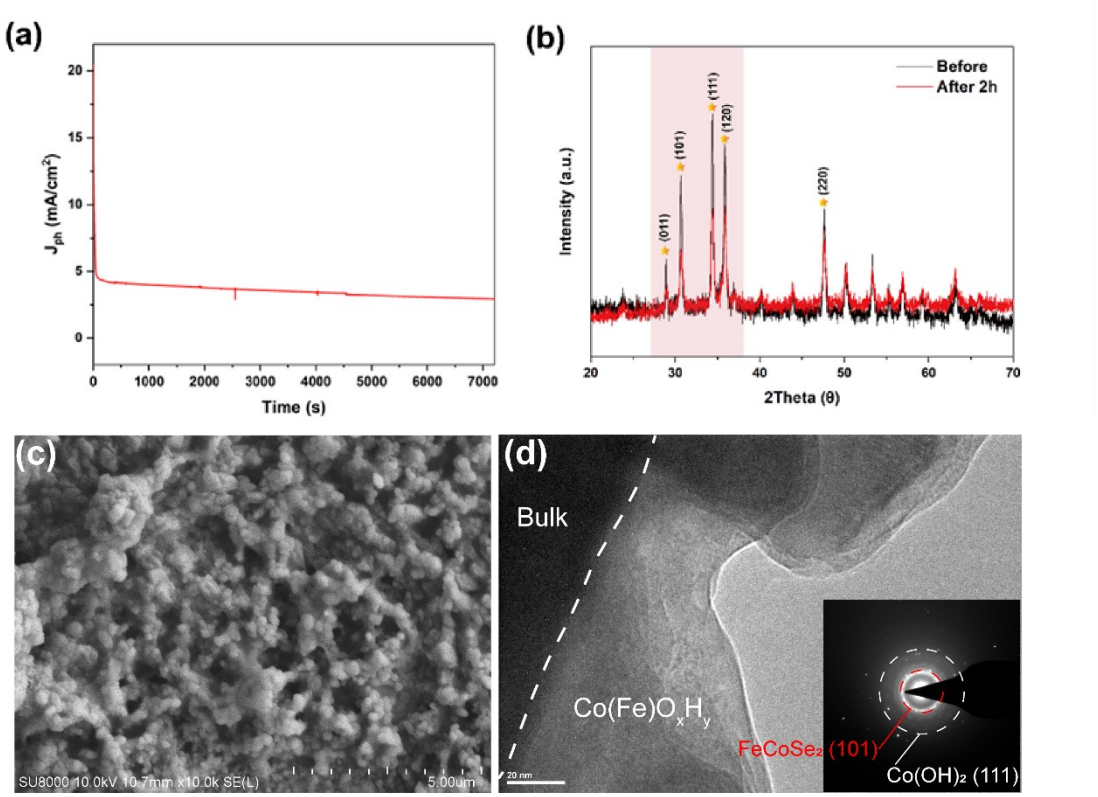

Figure. S11. (a)The stability test of $FeCoSe_2$ under 1.23 V vs RHE, AM 1.5G 100mW cm^{-2} and magnetic field. (b)The XRD of $FeCoSe_2$ after the stability test. (c) The SEM image of $FeCoSe_2$ after the stability test. (d) The TEM and SAED images of $FeCoSe_2$ after the stability test.

Unfortunately, due to photoelectrochemical corrosion, the performance of the material decreased to 81% within 2 hours. The decrease in performance can be attributed to the generation of $Co(Fe)O_xH_y$ (Figure S11c, d).

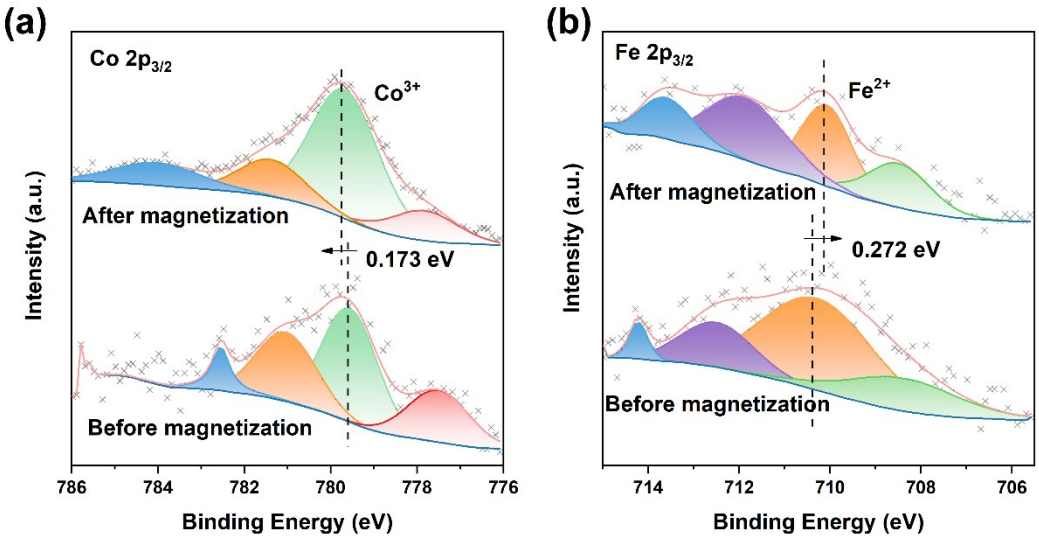

Figure. S12. (a, b) High resolution XPS spectra of Co $2p_{3/2}$, Fe $2p_{3/2}$ before and after magnetization.

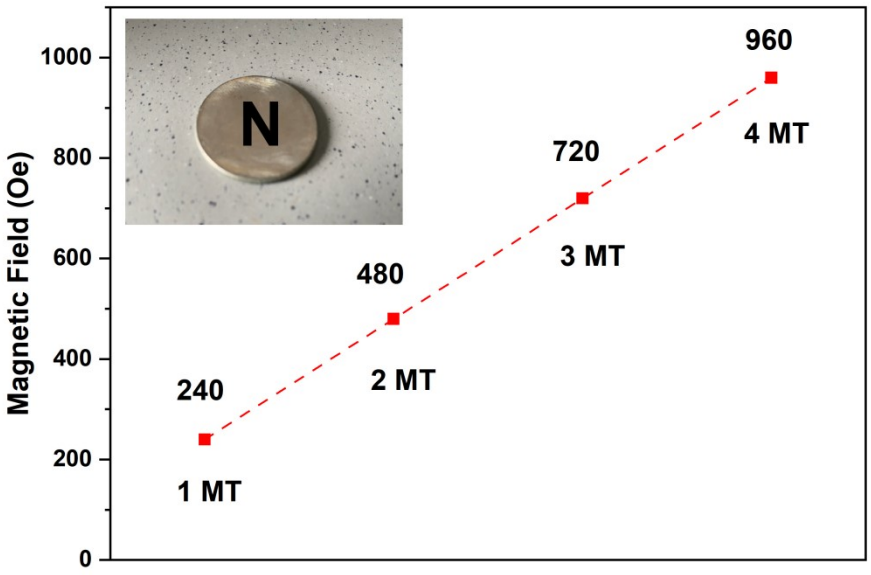

Figure. S13. Magnetic field strength provided by the magnet

The measured value is the strongest intensity at the center of the magnet and magnetic field strength test provided by the Manufacturer. The applied magnetic field photoelectrochemical performance tests covered in the article were performed at 4MT (Approximately equal to 960 Oe). When the magnetic field strength reaches 960 Oe, the material magnetization is approximately 56.27 emu g^{-1}.

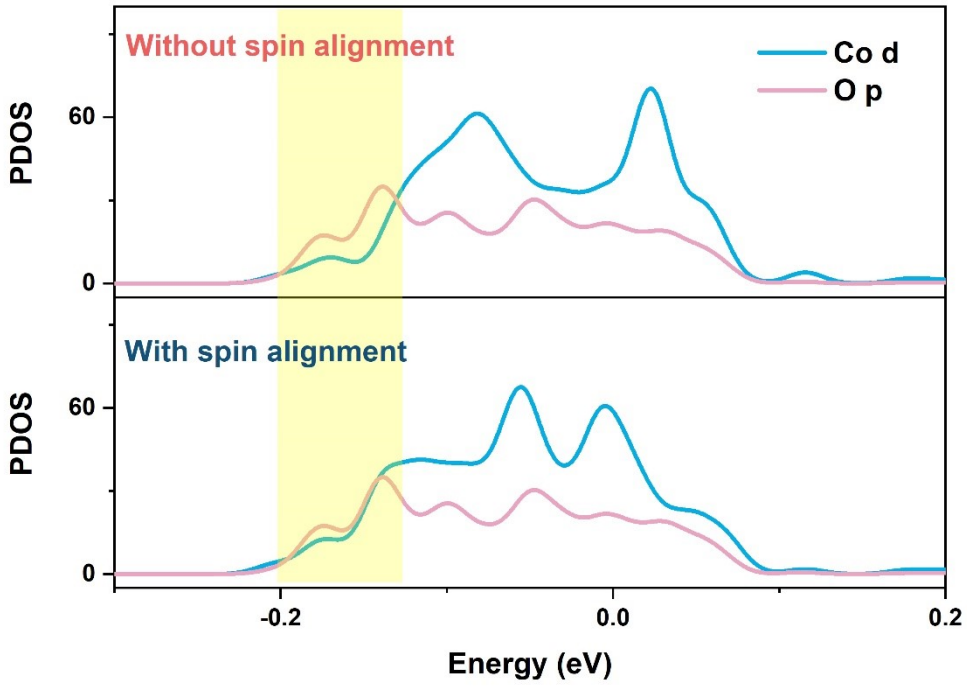

Figure. S14. The partial density of states of Co 3d and O 2p in different spin alignment state.

Table. S1 The structural information of $FeCoSe_2$ / $CoSe_2$ / $FeSe_2$.

$FeCoSe_2$	Space group: Pnnm						
	a	b	c	alpha	beta	gamma	volume
	4.854514	5.839789	3.63463	90	90	90	103.039
	elem	mult	x	y	z	Occupancy	Thermal Factor
	Co	2	0	0	0	0.572	0.025
	Se	4	0.2183	0.3672	0	1	0
	Fe	2	0	0	0	0.428	0.025
$CoSe_2$	Space group:Pnnm						
	a	b	c	alpha	beta	gamma	volume
	4.85413	5.838242	3.63524	90	90	90	103.021
	elem	mult	x	y	z	Occupancy	Thermal Factor
	Co	2	0	0	0	1	0.01
	Se	4	0.2183	0.3672	0	1	0
$FeSe_2$	Space group:Pnnm						
	a	b	c	alpha	beta	gamma	volume
	4.826368	5.800273	3.578883	90	90	90	100.188
	elem	mult	x	y	z	Occupancy	Thermal Factor
	Fe	2	0	0	0	1	0.003
	Se	4	0.2183	0.3672	0	1	0

Table. S2 Performance Comparison for Photoelectrocatalytic Water Splitting

	T (K)	emu/g （20k Oe）	Electrolyte	V vs RHE	J_{mph}	
$FeCoSe_2$	300	85.2	1M KOH	1.23	3.98 mA/cm^2	This Work
P-$ZnFe_2O_4$	300	8.6	1M KOH	1.57	1.06 mA/cm^2	[2]
3R-$AgFeO_2$	2	2.94	1M KOH	1.23	23.91 μA/cm^2	[3]
α-Fe_2O_3/rGO	300	0.45	1M NaOH	1.23	12.50 μA/cm^2	[4]
7.5 BFCO	300	2.62	0.1 M Na_2SO_4	1.23	15.00 μA/cm^2	[5]

References

1. X. Ren, T. Wu, Y. Sun, Y. Li, G. Xian, X. Liu, C. Shen, J. Gracia, H.-J. Gao, H. Yang and Z. J. Xu, *Nature Communications*, 2021, DOI: 10.1038/s41467-021-22865-y.
2. W. Gao, R. Peng, Y. Yang, X. Zhao, C. Cui, X. Su, W. Qin, Y. Dai, Y. Ma, H. Liu and Y. Sang, *ACS Energy Letters*, 2021, **6**, 2129-2137.
3. X.-D. Dong and Z.-Y. Zhao, *Journal of Materials Chemistry A*, 2022, **10**, 4800-4816.
4. J. Li, Q. Pei, R. Wang, Y. Zhou, Z. Zhang, Q. Cao, D. Wang, W. Mi and Y. Du, *ACS Nano*, 2018, **12**, 3351-3359.
5. C. Ponraj, P. S. Kumar, S. Sarkar, C. Krishnamoorthi, N. Manikandan, G. Vinitha and J. Daniel, *Surfaces and Interfaces*, 2022, **31**.